Understanding fracture mode-mixity and its effects on bond performance

Blackman, Bamber; Sun, Fengzhen; Teixeira de Freitas, Sofia; de Barros, Silvio; Moreira Arouche, Marcio; Ivankovic, Alojz

Important note
To cite this publication, please use the final published version (if applicable).
Please check the document version above.

Understanding fracture mode-mixity and its effects on bond performance

17

Bamber Blackman[a], Fengzhen Sun[b], Sofia Teixeira de Freitas[c], Silvio de Barros[d], Marcio Moreira Arouche[c], and Alojz Ivankovic[e]

[a]Department of Mechanical Engineering, Imperial College London, South Kensington Campus, London, United Kingdom, [b]Tongji University, Shanghai, China, [c]Aerospace Structures and Materials Department, Faculty of Aerospace Engineering, Delft University of Technology, Delft, Netherlands, [d]LINEACT CESI Engineering School, Paris, France, [e]University College Dublin, Dublin, Ireland

17.1   Introduction

The use of structural adhesives to join engineering components and structures has become very popular due to the many advantages structural adhesive bonding brings. These advantages include the avoidance of the need to drill holes or introduce local damage to the adherends, the improved stress distribution of adhesively bonded joints compared with mechanically fastened or welded joints, the ability to join dissimilar adherends and the improvement in structural rigidity, the reduction of vibration, and improved fatigue resistance, all of which make structural adhesive bonding a very highly employed joining technique.

To optimize joint performance, many studies [1,2] have shown that tensile opening forces (mode I) should be minimized and that in-plane shear forces (mode II) should be maximized, hence tensile butt joints are typically avoided in design, and joints loaded in shear such as the single- or double-lap joint are preferred. To further optimize joint performance, the stress concentrations associated with the ends of the joint overlap should be reduced by employing tapered adherends.

To measure adhesive joint performance, extensive use has been made of fracture mechanics since the pioneering initial studies by Ripling, Mosovoy, and Patrick in the 1960s [3]. Their work focused mainly on mode I loading of joints employing metallic adherends and led to the popular ASTM standard [4]. As structural joint designs were improved, there was increased interest in mode II and mixed-mode loading (i.e., combinations of modes I, II, and III acting together) and many workers explored test methods that combined modes, most commonly modes I and II. Although there have been many notable contributors to the understanding of the mixed-mode fracture behavior in adhesive joints such as [5–7], there is a lack of standardized tests developed specifically for these structures.

To analyze mixed-mode fracture tests, most workers have followed the energy release rate (G) approach and have combined this with beam theory methods to determine the rate of change of compliance C with crack length a, that is, to determine dC/da. This is then combined with the Irwin-Kies equation [8] to calculate the critical value of G for fracture, G_c. Initially, linear elastic fracture mechanics (LEFM) theory was followed, where one assumption is that any in-elastic deformation is limited in size to a very small zone at the crack tip and that the specimen behaves in a linear-elastic manner overall. Such assumptions are valid for brittle adhesives, but as adhesives have been manufactured with greatly improved toughness or ductility, the size of the in-elastic deformation zone at the crack tip has greatly increased, requiring the use of cohesive zone models to combine the approaches of fracture mechanics and classical strength of materials. The use of cohesive zone models and the concept of the cohesive zone length (damage length) have become increasingly important in the analysis of fracture in adhesively bonded joints under mixed-mode loading, as will be discussed in more detail later in this chapter as well as in Chapter 32 with digital image correlation (DIC) methods.

17.2   Brief summary of test methods to introduce mixed-mode loading

The accurate measurement of the fracture energy (G_c) is one key research campaign for characterization of the fracture behavior of laminated composites and adhesively bonded joints. Over the last few decades, many methodologies and data reduction schemes have been proposed to quantify the fracture energy for mode I, mode II, and mixed I/II mode loading [9]. Double cantilever beam (DCB) specimens loaded with pure bending moments provide a very accurate and robust way to determine the mode I fracture toughness (G_{Ic}) without the need for measuring crack lengths; however, this method does rely on the use of a specially designed loading jig [10]. Instead, specimens loaded with a transverse load are more often adopted, but this gives rise to the problem that the crack length must be determined. To measure the mode II fracture toughness (G_{IIc}), end notched flexure (ENF) tests using a three-point bending apparatus are extensively employed due to the test convenience; however, the crack growth in the specimens is intrinsically unstable and thus only initiation values of G_{IIc} are usually obtained [11]. Another way to determine the value of G_{IIc} is by using the end-loaded split (ELS) specimen, which is tested in a sliding clamp that only allows the specimen to slide freely in the horizontal direction, and the crack growth is relatively stable [12]. In addition, prior to the ELS test, a correction to the end clamping needs to be determined [12].

In practice, very rarely does failure in engineering structures occur under pure mode loading conditions. Crack growth under a combination of opening and shear modes is more commonly encountered, making it necessary to characterize the fracture behavior of structural adhesive joints under mixed-mode loading. The mixed mode flexure (MMF) specimen, also known as the single leg bending (SLB) specimen, and the fixed ratio mixed mode (FRMM) specimen are convenient choices to

complement the results obtained with the pure mode tests. The MMF configuration is very similar to the ENF test, and it is tested using a three-point bending rig, but only the upper arm at one end of the specimen is loaded. The FRMM test employs the same clamping arrangement as the mode II ELS test, but only one arm is loaded in this case. Symmetric MMF and FRMM specimens yield a constant mode-mixity G_{II}/G of 3/7.

Apart from the constant mode-mixity tests, a range of mode-mixity can be obtained by altering the relative thickness of the substrates such as the asymmetric DCB (ADCB) and asymmetric FRMM (AFRMM) specimens, although this raises the question of how to partition the mode-mixity correctly; this will be discussed in detail in the following section. The ADCB and AFRMM specimens are the generalization of the standard DCB and FRMM specimens using different beam thicknesses or different materials for the substrates. The specimens are manufactured and tested in the same manner as the DCB and FRMM tests. ADCB specimens are simpler to test than AFRMM specimens, but the achievable range of mode-mixity is much more limited in the ADCB than in the AFRMM case.

Another strategy to induce mixed-mode fracture is loading a symmetric adhesive joint with an apparatus designed to apply different load combinations such as those used in mixed-mode bending (MMB) [13], Arcan fixtures [14], and the rig developed by Fernlund and Spelt [15]. The MMB test is the only standardized mixed-mode I/II test available [16]. Although this standard was initially developed for unidirectionally fiber-reinforced polymer (FRP) composites, it has been successfully used to test multidirectional FRPs and adhesive joints. The MMB test covers a wide range of mode I to mode II loadings by adjustment of the loading and lever fulcrum positions in the test apparatus [13]. This type of test combines opening and in-plane sliding displacement modes, and the applied loading usually is treated as the superposition of the applied loadings of the DCB and ENF tests. Its advantage is that a range of mixed-mode I/II load cases can be studied without having to change the specimen geometry, but it does require a complex fixture and bonded steel hinged tabs, which may introduce a geometrical nonlinearity.

Another mixed-mode loading apparatus was introduced by Fernlund and Spelt [15]. The load jig consists of a link-arm system that allows the force acting on the upper and lower substrates of the test specimen to be varied by altering the load jig geometry. The links in the load jig are connected to each other with dowel pins to facilitate the geometry change. The nominal phase angle of loading is independent of the specimen crack length, and it also allows mode ratios from pure mode I to pure mode II to be obtained. Important features are that all mixed-mode ratios can be generated with a single equal-adherend DCB specimen, and the mixed-mode ratio is independent of crack length. Recently, Costa et al. [17] developed a more compact apparatus based upon the Fernlund and Spelt method. These authors demonstrated, using mixed-mode and classical models (ATDCB, SLB, DCB, and ENF), the validity of the results obtained with the new apparatus.

Arcan et al. [14] proposed a biaxial fixture, commonly known as the Arcan fixture, to produce biaxial states of stress. The compact nature of the Arcan fixture enables the shear properties in all in-plane directions to be obtained in a relatively simple manner. Various mixed-mode combinations can be achieved by rotating the loading direction.

However, although the Arcan test covers all the mixed-mode ratios, including the pure mode I to mode II, the results can only be obtained by a numerical (finite element) analysis, which involves the singularity at the crack tip. The cracked-lap shear (CLS) was also an attempt to construct a mixed-mode testing approach, and it was popular for fatigue testing in the aerospace industry because of its nominally constant energy release rate as a function of debonding length [18]. However, one distinctive feature of the CLS is the eccentric loading path that leads to geometrical nonlinearity, as was identified in the ASTM round-robin activity [19]. Thus, large deflections have to be considered in analytical and numerical analyses. Due to these limitations, other tests have become more popular.

Finally, mixed-mode loading of adhesive joints or interfaces has been achieved via the use of dual actuator loading frames [7,20,21], where the loading of each specimen arm is independently controlled. Challenges here include the maintenance of a constant mode-mixity during quasistatic tests [20] and the maintenance of constant local separation rates with changing mode-mixity in higher rate tests [21].

17.3 Mixed-mode partitioning schemes

17.3.1 Introduction

The mixed-mode loading situation raises fundamental questions that are not relevant to the pure mode case. For example, to what extent do the two loading modes interact when applied simultaneously to modify the resistance of the joint from that which would be predicted from a simple linear addition of the separate mode contributions? Indeed, it is frequently observed that such a linear addition is a poor descriptor of mixed-mode fracture resistance, and that a stronger interaction exists [22]. So, to define the correct degree of interaction (fracture criterion), it is important to be able to partition the total loading correctly into its constituent parts. In terms of fracture energy, the mixed-mode fracture resistance G_c must be partitioned into the mode I and mode II components.

17.3.2 Local and global partitioning schemes for monolithic specimens

Attempts to partition mixed-mode loading into pure mode components have traditionally taken either a local or a global approach. In the local approach, the stress singularity at the crack tip is assumed to control fracture. This requires that the region controlled by the singular field (K-dominant zone) engulfs the crack tip process zone (plastic and/or damage zone). The singular field stress distributions are determined at the crack tip and these are partitioned into the mode I and II components, K_I and K_{II}, which can then be written in terms of the associated energy release rate components, G_I and G_{II}, respectively. In the global approach, the bending moments applied to the specimen are considered but the details of the local stress or strain fields ahead of the crack tip are neglected. Williams [23] proposed that these applied moments could be

partitioned into components that induce pure mode I (M_I) and pure mode II (M_{II}). Fig. 17.1 shows a cracked beam-like geometry subjected to pure bending moments of M_1 on the upper beam and kM_1 on the lower beam [24]. The upper beam has a thickness of h_1 and the lower beam a thickness of h_2, and the ratio of heights is $\gamma = h_1/h_2$.

Local and global partitioning approaches have been reviewed by Conroy et al. [24], and an application of the global approach is discussed further in Section 17.4. As is shown in Fig. 17.2a, when the test specimen has a symmetric geometry, as is the case for the mixed-mode bending (MMB) specimen, then the local and global partitioning approaches produce identical results for the applied mixed-mode partition ratio, G_{II}/G. Note that for $\gamma = 1$, when the applied moment ratio $k = -1$, then pure mode I loading is obtained and when $k = 1$, then pure mode II is obtained. However, as is shown in Fig. 17.2b, for an asymmetric geometry, in this case the AFRMM specimen, then the local and global partitioning approaches produce very different results. Fig. 17.2b shows the mixed-mode partition ratio G_{II}/G as a function of the beam height ratio γ, where the two approaches only agree when $\gamma = 1$. It is noteworthy therefore that if only symmetric specimens are used, the two partitioning approaches produce identical results in monolithic specimens.
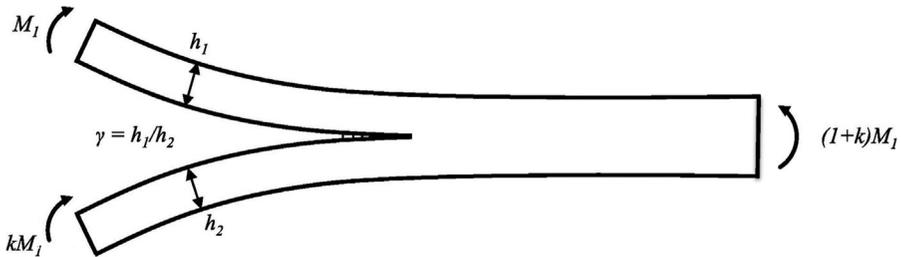

Fig. 17.1 Beam-like geometry subjected to pure bending moments (M_1 and kM_1) [24].
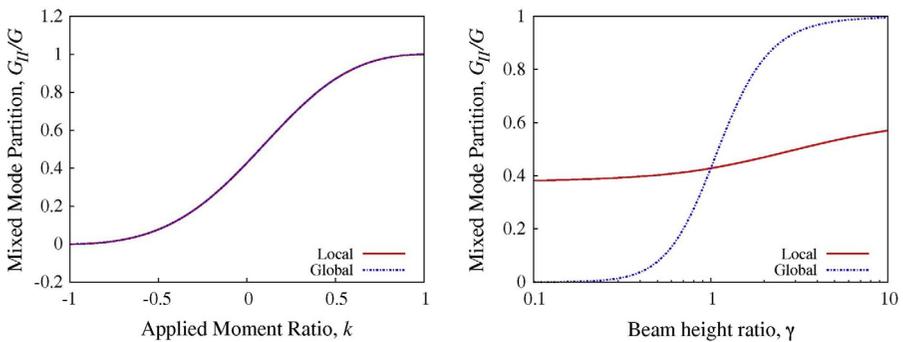

Fig. 17.2 Local and global partitioning: (a) symmetric specimens such as MMB; (b) asymmetric specimens such as AFRMM [24].

17.3.3   A damage-based partitioning scheme

For highly fracture-resistant materials, including joints bonded with toughened adhesives, the length of the fracture process zone (the cohesive zone) can be significantly larger than the extent of the singular field. For these materials, the global approach has traditionally found greater success. Conroy et al. [24] noted from their numerical studies that as the degree of damage increased, that is, as the size of the cohesive zone increased, then the global partitioning approach becomes more accurate. Conversely, as the amount of damage decreased, then the local partitioning approach becomes more accurate. Conroy et al. [24] proposed a damage-dependent partitioning method that was termed the semianalytical cohesive analysis (SACA), which is now discussed.

Conroy et al. [24] proposed that the partitioning approach should acknowledge the state of damage in the specimen. They allowed this to be scaled via a singularity factor f between a lower bound given by the local solution and an upper bound given by the global solution, where f was given by:

$$f = \frac{\left(\frac{G_{II}}{G}\right) - \left(\frac{G_{II}}{G}\right)_{W}}{\left(\frac{G_{II}}{G}\right)_{HS} - \left(\frac{G_{II}}{G}\right)_{W}} \tag{17.1}$$

where $(G_{II}/G)_{W}$ and $(G_{II}/G)_{HS}$ are the mixed-mode ratios given by the global and local solutions, respectively, and (G_{II}/G) is the predicted mixed-mode partition ratio according to this semianalytical cohesive analysis (SACA) method. To employ the SACA method, a normalized damage length parameter was defined for the specimen, l_{nd}, where this is given by:

$$l_{nd} = \frac{l_{cz}}{a_{c}} \tag{17.2}$$

where l_{cz} is the cohesive zone length and a_{c} is the smallest characteristic dimension of the specimen. The cohesive zone lengths in modes I and II were determined analytically and the singularity factor was then given by Eq. (17.3) or (17.4), depending upon whether the value of l_{nd} was less than 0.3.

$$f = 1 \text{ if } l_{nd} \leq 0.3 \tag{17.3}$$

$$f = 0.9682\mathrm{e}^{-0.24l_{nd}} + 0.0983\mathrm{e}^{-0.2l_{nd}} \text{ otherwise} \tag{17.4}$$

Based upon Eqs. (17.3) and (17.4), partitioning via the local singular field approach was considered accurate for cohesive zone lengths up to 30% of the smallest characteristic length. The singularity factor f was dependent upon material properties and specimen geometry. Conroy et al. [24] applied the method to various test cases based upon composite materials in the literature with excellent results. The method is evaluated for a structural adhesive joint in the next section.

17.3.4 Evaluation and discussion of mixed-mode partitioning

Mixed-mode partitioning schemes were investigated experimentally by Alvarez et al. [25] for structural adhesive joints in which carbon fiber-reinforced composite adherends had been bonded with a toughened aerospace film adhesive grade AF163-2 OST. These authors employed various test specimens, including ADCB, FRMM, and AFRMM. The experimental results were partitioned according to the global approach and according to two forms of the local approach: the first one based on the crack tip element (CTE) method of Davidson et al. [26], which was termed the singular field (CTE-SF), and the second method was a nonsingular field (CTE-NSF) version of Davidson's method. They also explored the use of the SACA method.

Alvarez et al. [25] found that for this relatively tough adhesive joint, the global partitioning approach [23] was generally accurate across the range of mixed-mode ratios (G_{II}/G) attained, but showed the largest percentage errors at the smallest mixed-mode ratios. Additionally, as has frequently been noted in the literature, the global partitioning approach is anomalous for the ADCB test, where it predicts $(G_{II}/G)=0$, that is, mode I, for all arm thickness ratios. The local approach via Davidson's CTE-SF method was accurate at the smallest mixed-mode ratios and Davidson's CTE-NSF method was accurate at intermediate ratios, but both became nonphysical at higher mixed-mode ratios, such as for $(G_{II}/G)>0.5$. The SACA method, in which the singularity factor f was determined for the adhesive joint based upon the material properties of the adhesive and the adherends and the specimen geometry, gave the most accurate mixed-mode partitioning across the entire range $0<(G_{II}/G)\leq1$. In Fig. 17.3, the mixed-mode failure envelope was
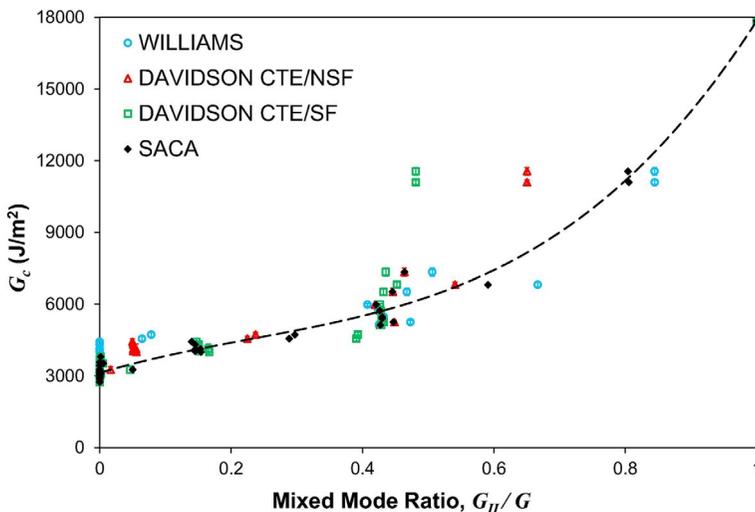

Fig. 17.3 Comparison of the failure locus obtained from the experimental results partitioned via the global approach (Williams [23]); the singular and nonsingular field versions of Davidson's analysis, CTE/NSF and CTE/SF; and the SACA method [25].

drawn using the B-K criterion. Note that failure envelopes are discussed in more detail in Section 17.5 of the present chapter.

17.4 Application of global partitioning to mixed-mode bi-material interface joints

In this section, the mixed-mode fracture behavior of a bi-material adhesively bonded joint is investigated. The strain-based method (SBM) is described, evaluated, and tested on a composite-to-metal bonded joint using the MMB test.

17.4.1 Analytical framework: Introducing the longitudinal strain-based criterion

17.4.1.1 Strain energy release rate

The strain energy release rate (SERR) is one of the most important parameters to consider for characterizing the fracture behavior of cracked structures. For linear elastic behavior, the total SERR can be obtained by the balance of fracture energy through the following equation:

$$G = \frac{1}{B}\left(\frac{\delta U_e}{\delta a} - \frac{\delta U_s}{\delta a}\right) \tag{17.5}$$

where B is the width of the specimen, U_e is the external work performed, U_s is the strain energy, and a is the crack length. The analysis considers a region ABCD mechanically affected by the presence of a crack under pure bending moments, as shown in Fig. 17.4.

The upper and lower arm thicknesses are h_1 and h_2, and the bending moments applied to the upper and lower arms are M_1 and M_2, respectively. The angles Φ_0, Φ_1, and Φ_2 represent the slopes of the beam, upper arm, and lower arm, respectively. When the crack grows a length δa from O on section AB to O′ on section CD, the external work is:
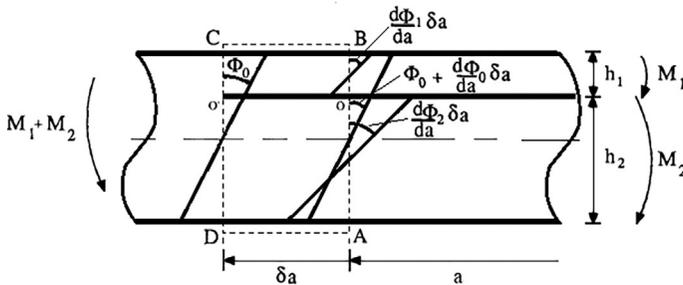

Fig. 17.4 Beam analysis under pure bending moments [27].
Reprinted with permission from Taylor & Francis Ltd, http://www.tandfonline.com.

$$\frac{\delta U_e}{\delta a} = M_1 \left(\frac{\delta \phi_1}{\delta a} - \frac{\delta \phi_0}{\delta a} \right) + M_2 \left(\frac{\delta \phi_2}{\delta a} - \frac{\delta \phi_0}{\delta a} \right) \tag{17.6}$$

For pure bending, the change in angle is given by:

$$\frac{\delta \phi}{\delta a} = \frac{M}{EI} \tag{17.7}$$

where M is the moment, E is the flexural modulus, and I is the second moment of area. Similarly, the strain energy is:

$$\frac{\delta U_s}{\delta a} = \frac{M_1^2}{2E_1 I_1} + \frac{M_2^2}{2E_2 I_2} - \frac{(M_1 + M_2)^2}{2E_{eq} I_{eq}} \tag{17.8}$$

where E_1, I_1, E_2, I_2, E_{eq}, and I_{eq} are the flexural longitudinal moduli and second moments of the area in the section of the crack tip of the upper arm, lower arm, and total specimen, respectively. Substituting Eqs. (17.6) and (17.8) in Eq. (17.5), it can be reduced to the equation of the total fracture energy:

$$G = \frac{1}{2B} \left(\frac{M_1^2}{E_1 I_1} + \frac{M_2^2}{E_2 I_2} - \frac{(M_1 + M_2)^2}{E_{eq} I_{eq}} \right) \tag{17.9}$$

Eq. (17.9) allows determining the total fracture energy released from a crack between two arms. However, it is essential for the characterization of the mechanical behavior to define the contribution of mode I and mode II fracture.

17.4.1.2 Williams' global partitioning approach

In the late 1980s, Williams [23] proposed a fracture partitioning method (WM) based on the assumptions that: (i) pure mode I exists when opposite moments act on the joint arms; and (ii) pure mode II is obtained when the curvatures of the two arms are the same. This means:

$$M_1 = M_{II} - M_I \tag{17.10}$$

$$M_2 = \psi M_{II} + M_I \tag{17.11}$$

Where the bending stiffness ratio between upper and lower arms is:

$$\psi = \frac{E_2 I_2}{E_1 I_1} \tag{17.12}$$

Substituting Eqs. (17.10) and (17.11) in Eq. (17.9), the equation of the total fracture energy can be reduced to:

$$G = \frac{1}{2B}\left[M_{\mathrm{I}}^2\left(\frac{\psi + 1}{E_2 I_2}\right) + M_{\mathrm{II}}^2\left(\frac{\psi + \psi^2}{E_2 I_2} - \frac{(1 + \psi)^2}{E_{\mathrm{eq}} I_{\mathrm{eq}}}\right)\right] \tag{17.13}$$

Notice that no cross-product term is observed. Therefore, the partitioning can be obtained by rewriting Eq. (17.13) as a function of M_{I} and M_{II}:

$$f(M_{\mathrm{I}}, M_{\mathrm{II}}) = f_{\mathrm{I}}(M_{\mathrm{I}}) + f_{\mathrm{II}}(M_{\mathrm{II}}) \tag{17.14}$$

G_{I}, G_{II}, and the total G are then given by:

$$G_{\mathrm{I}} = \frac{M_{\mathrm{I}}^2}{2B}\left(\frac{\psi + 1}{E_2 I_2}\right) \tag{17.15}$$

$$G_{\mathrm{II}} = \frac{M_{\mathrm{II}}^2}{2B}\left(\frac{\psi + \psi^2}{E_2 I_2} - \frac{(1 + \psi)^2}{E_{\mathrm{eq}} I_{\mathrm{eq}}}\right) \tag{17.16}$$

$$G = G_{\mathrm{I}} + G_{\mathrm{II}} \tag{17.17}$$

Finally, substituting Eqs. (17.10) and (17.11) in Eqs. (17.15) and (17.16), the mode I and mode II SERR can be written as:

$$G_{\mathrm{I}} = \frac{(\psi M_1 - M_2)^2}{2B(\psi + 1)^2}\left(\frac{1}{E_1 I_1} + \frac{1}{E_2 I_2}\right) \tag{17.18}$$

$$G_{\mathrm{II}} = \frac{(M_1 + M_2)^2}{2B(\psi + 1)}\left(\frac{1}{E_1 I_1} - \frac{(\psi + 1)}{E_{\mathrm{eq}} I_{\mathrm{eq}}}\right) \tag{17.19}$$

Analytical models based only on simple beam analysis do not properly describe the crack propagation mechanism [28]. The two arms are not fixed against rotation at the crack tip, as assumed in the beam analysis. To account for these effects in the mode I fracture, Williams [29] proposed a correction factor, based on Kanninen's [30] elastic foundation model. Then, Wang and William [31] extended the same correction factor for the mode II fracture component. The incorporation of crack tip correction factors in the beam model, Eqs. (17.18) and (17.19), resulted in the so-called corrected beam theory (CBT). In this method, an effective crack length is used to account for the contribution of shear deformation to the energy release rate.

The works of Williams [22], Hashemi et al. [32], and Ducept et al. [33] indicated that CBT produces reliable values for the total fracture energy and partitioning ratio of symmetric cracks. However, Ducept et al. [34] showed that WM does not provide reliable results of the fracture mode partitioning of cracks between asymmetric arms. The assumptions for the pure modes do not describe with precision the interaction between mode I and mode II fractures. Therefore, it is not recommended for the characterization of asymmetric cracks.

17.4.1.3 Strain-based partitioning method

Arouche et al. [27,35] introduced a new criterion for fracture mode partitioning, the strain-based partitioning method (SBM). The main difference to the WM lies on the condition for pure mode I: it incorporates the requirement of strain equivalence between the faying surfaces for ensuring pure mode I, as identified by Ouyang [36] and confirmed by Wang et al. [37]. In the case of pure mode II, similarly to WM, the SBM assumes that it is produced when both arms have the same curvature, as observed by Mollón et al. [38], assuming that the curvature of the neutral axis is the same as the faying surfaces. Therefore, the partitioning assumptions become: (i) the longitudinal strain distribution at the faying surfaces of both arms must be identical to produce pure mode I, and (ii) pure mode II is obtained when the curvature in the two arms is the same. This gives:

$$M_1 = M_{II} - M_I \tag{17.20}$$

$$M_2 = \psi M_{II} + \beta M_I \tag{17.21}$$

Where the longitudinal strain ratio between upper and lower arms is:

$$\beta = \frac{E_2 h_2^2}{E_1 h_1^2} \tag{17.22}$$

Substituting Eqs. (17.20) and (17.21) in Eq. (17.9), the total SERR is obtained:

$$G = \frac{1}{2B} \left[\begin{array}{c} M_I^2 \left(\dfrac{\psi + \beta^2}{E_2 I_2} - \dfrac{(\beta - 1)^2}{E_{eq} I_{eq}} \right) + M_{II}^2 \left(\dfrac{\psi + \psi^2}{E_2 I_2} - \dfrac{(1 + \psi)^2}{E_{eq} I_{eq}} \right) + \\ M_I M_{II} \left(\dfrac{2\psi\beta - 2\psi}{E_2 I_2} - \dfrac{2(1 + \psi)(\beta - 1)}{E_{eq} I_{eq}} \right) \end{array} \right] \tag{17.23}$$

Eq. (17.23) shows that the mode I fracture energy affects the mode II fracture energy and vice versa. Consequently, the equation can only be written in the form of:

$$f(M_I, M_{II}) = f_I(M_I) + f_{II}(M_{II}) + f_c(M_I, M_{II}) \tag{17.24}$$

Eq. (17.24) displays a coupling function $f_c(M_I, M_{II})$ beyond the functions of pure mode I and pure mode II–$f_I(M_I)$ and $f_{II}(M_{II})$, respectively. This implies that the fracture mode partitioning is obtained when the coupling function $f_c(M_I, M_{II})$ is zero. This is achieved in the condition of $\beta = 1$. Therefore, the specimen design condition of longitudinal strain equivalence has to be satisfied. It means:

$$E_1 h_1^2 = E_2 h_2^2 \tag{17.25}$$

In this case, the mode I and mode II equations of fracture energy are the same as in WM—Eqs. (17.18) and (17.19). However, WM does not reinforce any specific specimen design because it was derived for symmetric specimens in which β is always equal to 1. It ignores the coupling function that contributes to the total fracture energy. This is the reason why WM is inaccurate if applied to asymmetric specimens where the longitudinal strain-based design criterion is not applied ($\beta \neq 1$).

17.4.2 Application in MMB test in composite-to-metal bonded joints

17.4.2.1 MMB test

Reeder and Crews [38] developed the MMB test as a combination of the DCB and the ENF tests. In the MMB test, a load (P) is applied through a roller attached to a lever and loaded just above the midplane of the test specimen. The test loading is decomposed into opening (P_I) and shear (P_{II}) loadings in a constant ratio determined by the lever length (c). The original procedure was later redesigned to minimize geometrical nonlinearity effects [39] and to take into account the weight of the lever (P_g) and the distance of the lever center of gravity (c_g) [40]. Later, Chen et al. [41] proposed a modification to the test apparatus to avoid preloading on the specimens caused by the weight of the lever. The MMB test scheme is shown in Fig. 17.5. The MMB test has proved to be an easy and reliable method for measuring a wide range of mixed-mode ratios with only one specimen geometry [33,42]. The loads applied to the specimen are shown in Fig. 17.6.

The resulting bending moments are:

$$M_1 = \frac{Pc + P_g c_g}{L} a \tag{17.26}$$

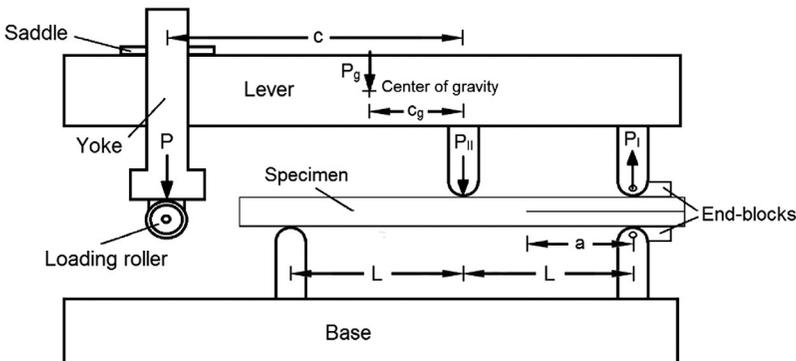$$M_2 = \frac{P(L - c) + P_g(L - c_g)}{2L} a \tag{17.27}$$
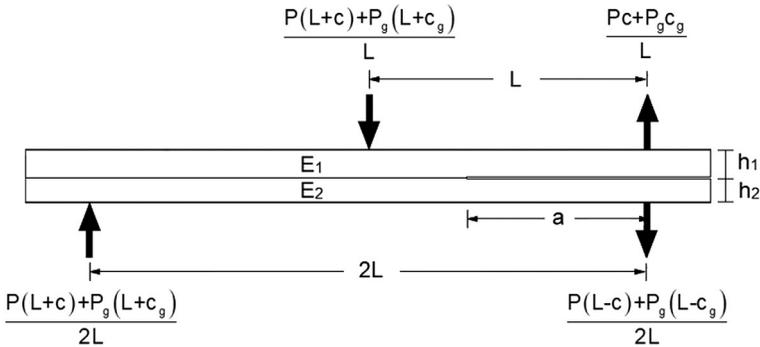

Fig. 17.5 MMB test scheme.

Fig. 17.6 MMB specimen free body diagram.

Then, the mode I and mode II SERR of an MMB test specimen can be obtained by replacing Eqs. (17.26) and (17.27) in Eqs. (17.18) and (17.19).

17.4.2.2 Numerical model

A virtual MMB test was chosen to evaluate the SBM. The geometric features of the two-dimensional (2D) model are a 70 mm half-span (L) and a 50 mm crack length (a). The upper and lower arm thicknesses (h_1 and h_2, respectively) and materials (E_1 and E_2, respectively) are the parameters varied in the analysis [27].

17.4.2.3 Asymmetric crack within the same material

The first parametric study was performed on an asymmetric crack within the same material. The upper and lower arms have the same elastic modulus (E_1 and E_2) of 70 GPa and a Poisson's ratio (ν_1 and ν_2) of 0.33. In order to verify the influence of the fracture mode ratio in the accuracy of the analytical methods, three different conditions were considered: low ($c=117$ mm), intermediate ($c=61$ mm), and high ($c=42$ mm) mode II ratio. Table 17.1 shows the three cases of geometrical asymmetry. The upper arm thickness (h_1) is varied in a wide range of geometries applied to the MMB test specimen while the lower arm thickness (h_2) remains at 3.0 mm. The crack length is kept at 50 mm and the test load (P) is 100 N.

Analytical and numerical results of the total fracture energy (G) are presented in Fig. 17.7. Fig. 17.7a–c show the three cases of low (case 1), intermediate (case 2),

Table 17.1 Study cases of geometrical asymmetry.

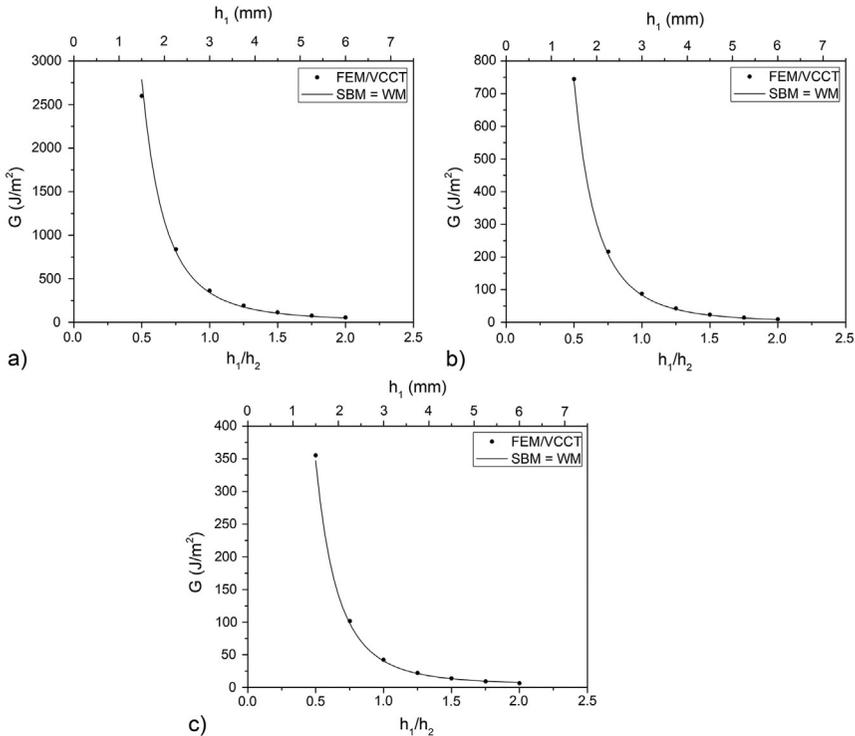| Case	Lever length, c (mm)	h_1 (mm)	h_2 (mm)	E_1; E_2 (GPa)	ν_1; ν_2
1	117	$1.5 < h_1 < 6.0$	3.0	70	0.33
2	61	$1.5 < h_1 < 6.0$	3.0	70	0.33
3	42	$1.5 < h_1 < 6.0$	3.0	70	0.33

Fig. 17.7 Total fracture energy with the variation of the specimen thickness: cases (a) 1—low, (b) 2—intermediate, and (c) 3—high mode II [27].
Reprinted with permission from Taylor & Francis Ltd, http://www.tandfonline.com.

and high (case 3) mode II fracture, respectively. Overall, the total fracture energy obtained from analytical solutions based on beam analysis are in very good agreement with the numerical results.

Fig. 17.8 shows the analytical and numerical fracture mode ratio (G_{II}/G). Notice that the SBM implies that the specimen design condition is satisfied ($\beta = 1$) and, for this condition, gives the same result of WM. Fig. 17.8a shows the results for low mode II (case 1). When $\beta = 1$, the specimen is symmetric in the crack plane ($h_1/h_2 = 1$) and both analytical methods show good agreement with numerical results. As β differs from 1, WM gives significant discrepancies from the FEM/VCCT results. This shows that WM is only valid for the condition $\beta = 1$. Similar results are observed as the mode II fracture ratio increases, in Fig. 17.8b and c (cases 2 and 3, respectively). Moreover, the limitation of WM to predict the fracture partitioning ratios on asymmetric cracks within the same material is noticeable. This can be explained by the influence of the mode I and mode II coupling on the fracture energy.

Table 17.2 shows the results and errors of the analytical model in comparison with the numerical model for the condition of symmetric crack. Slight errors between −4.2% and −6.0% are observed in the calculation of the total fracture energy and between 2.6% and 7.6% in the fracture mode ratio. In the particular condition of a symmetric crack, the literature suggests crack tip corrections to account for the effect of crack tip rotation under mode I [29] and mode II [31] fracture. The analytical
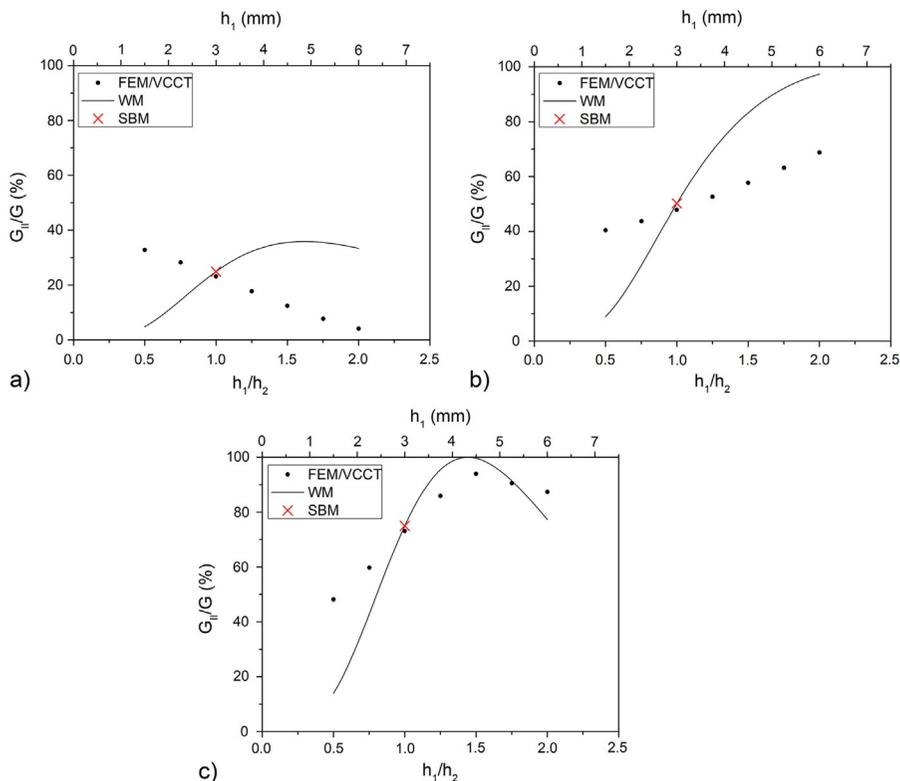
Fig. 17.8 Fracture mode ratio with the variation of specimen thickness: cases (a) 1—low, (b) 2—intermediate, and (c) 3—high mode II [27].
Reprinted with permission from Taylor & Francis Ltd, http://www.tandfonline.com.

Table 17.2 Results and errors of the analytical model in the condition of symmetric specimen in the crack plane.

Case	Numerical model G (J/ m²)	Numerical model G_{II}/ G (%)	Analytical model G (J/ m²)	Analytical model Error (%)	Analytical model G_{II}/ G (%)	Analytical model Error (%)	Analytical model with crack tip corrections G (J/ m²)	Analytical model with crack tip corrections Error (%)	Analytical model with crack tip corrections G_{II}/ G (%)	Analytical model with crack tip corrections Error (%)
1	362.3	23.2	340.7	−6.0	24.9	7.6	364.7	0.6	24.1	4.0
2	87.7	47.9	83.1	−5.2	50.2	4.8	87.9	0.3	49.1	2.5
3	42.4	73.1	40.6	−4.2	75.0	2.6	42.5	0.2	74.1	1.4

method with the application of these correction factors presented insignificant errors for the calculation of the total fracture energy and errors lower than 4.0% for the fracture mode ratio (see Table 17.2). In both cases, the use of correction factors resulted in more accurate results. This shows that the effect of crack tip rotation during the experiments may have a nonnegligible effect on the fracture behavior, although the simple analytical model proved to be reliable.

17.4.2.4 Bi-material crack

A second parametric study was carried out on a crack at a bi-material interface with asymmetric geometry. The upper arm has a thickness (h_1) of 2.12 mm and the lower arm has a thickness (h_2) of 3.0 mm. To verify the influence of the fracture mode ratio in the accuracy of the analytical methods, three different conditions were considered: low ($c = 95$ mm), intermediate ($c = 49$ mm), and high ($c = 34$ mm) mode II ratio. Table 17.3 shows the three cases of bi-material crack. The upper arm elastic modulus (E_1) is varied in a wide range of reasonable materials applied to MMB test specimens. The lower arm has an elastic modulus (E_2) of 70 GPa and both arms have a Poisson's ratio (ν_1 and ν_2) of 0.33. The crack length is kept at 50 mm and the test load (P) is 100 N, likewise the previous cases.

Analytical and numerical results of the total fracture energy (G) are presented in Fig. 17.9. Both analytical methods give the same results for any material. Fig. 17.9a, b, and c show the three cases of low, intermediate, and high mode II fracture, respectively. Both analytical methods are in very good agreement with the FEM/VCCT results, hence, the analytical methods based on beam analysis provide reliable results of the total fracture energy on bi-material cracks.

Fig. 17.10 shows the analytical and numerical fracture mode ratio (G_{II}/G). For the applied parameters, the strain-equivalent geometry ($\beta = 1$) is achieved when E_1/E_2 equals 2.0. In the case of low mode II (case 4), shown in Fig. 17.10a, the SBM shows good agreement with the FEM/VCCT despite the remarkable asymmetry of the materials and geometry. However, as β differs from 1, WM gives significant discrepancies from the FEM/VCCT results. This shows that the analytical method based on beam analysis is only valid for when the strain-equivalence condition is respected. Similar results are observed as the mode II fracture ratio increases, presented in Fig. 17.10b and c (cases 5 and 6, respectively). Moreover, it is shown once more that WM only predicts accurate fracture mode ratios when the condition of strain equivalence is satisfied ($\beta = 1$). For any other geometry, the coupling effect between fracture modes is not taken into account and therefore incorrectly predicts the fracture mode ratios. The influence of the mode I and mode II coupling may have a large effect on the fracture mode of bi-material cracks. This reinforces the requirement of the strain-based design criterion for obtaining the correct partitioning ratio.

Table 17.4 shows the results and errors of the analytical model in comparison with the numerical model for the particular condition of strain equivalence proposed in the SBM (see Eq. (17.23)). Errors between 1.0% and −8.1% are observed in the calculation of the total fracture energy and between 1.1% and −8.6% in the fracture mode

Table 17.3 Study cases of a crack at a bi-material interface.

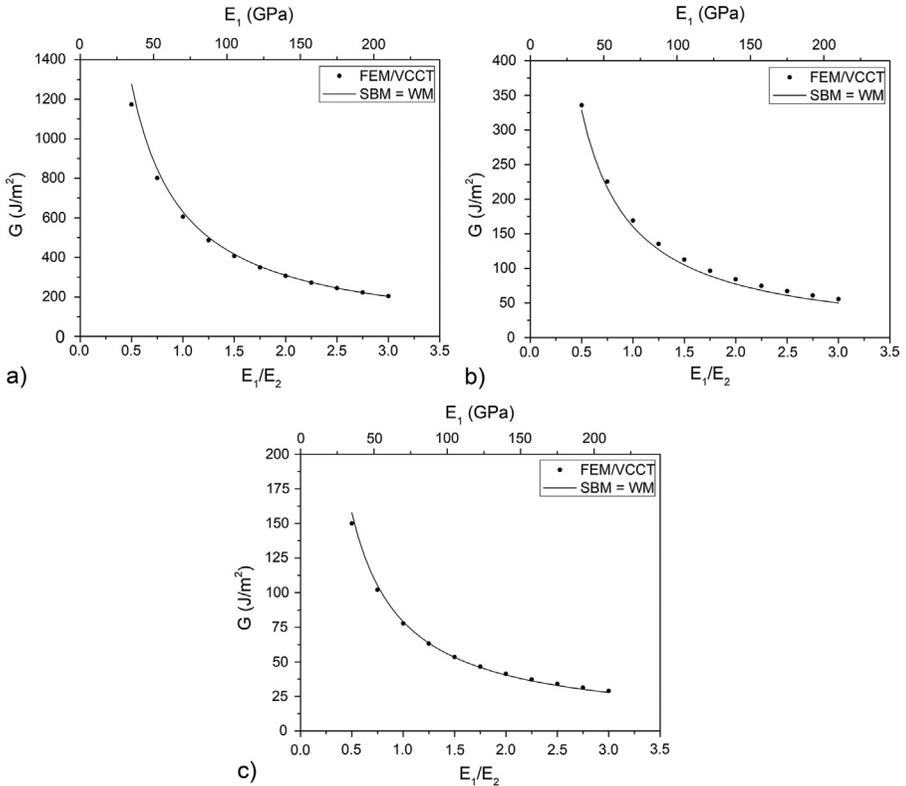| Case	Lever length, c (mm)	h_1 (mm)	h_2 (mm)	E_1 (GPa)	E_2 (GPa)	ν_1; ν_2
4	95	2.12	3.0	$35 \leq E_1 \leq 210$	70	0.33
5	49	2.12	3.0	$35 \leq E_1 \leq 210$	70	0.33
6	34	2.12	3.0	$35 \leq E_1 \leq 210$	70	0.33

Fig. 17.9 Total fracture energy with the variation of the specimen material: cases (a) 4—low, (b) 5—intermediate, and (c) 6—high mode II [27].
Reprinted with permission from Taylor & Francis Ltd, http://www.tandfonline.com.

ratio. These errors are in a similar degree as cases 1, 2, and 3 of symmetric condition, presented in Table 17.2. Therefore, it can be implied that the effect of crack tip rotation is also a major cause of the errors produced in cases 4, 5, and 6 of bi-material cracks using the SBM.

17.4.2.5 Application of the SBM to composite-to-metal bonded joints

To evaluate the SBM and validate the previous numerical analysis, a test campaign has been conducted in which MMB tests were performed [27,35]. Composite-to-metal bonded joints were manufactured in thin and thick geometries. The geometry of the joint was designed to satisfy the criterion of strain equivalence ($\beta=1$). The mechanical properties of the materials are shown in Table 17.5.

Table 17.6 shows the test matrix. The half-span (L) of the test is 70 mm and the initial crack length (a_0) of 30 mm was obtained after bonding the end blocks.

The total fracture energy and mode ratio were obtained at crack propagation using the SBM and the FEM assuming cohesive failure in the adhesive. Fig. 17.11a and b show the total fracture energy of Tests 1 and 2 in thick specimens. The SBM produced
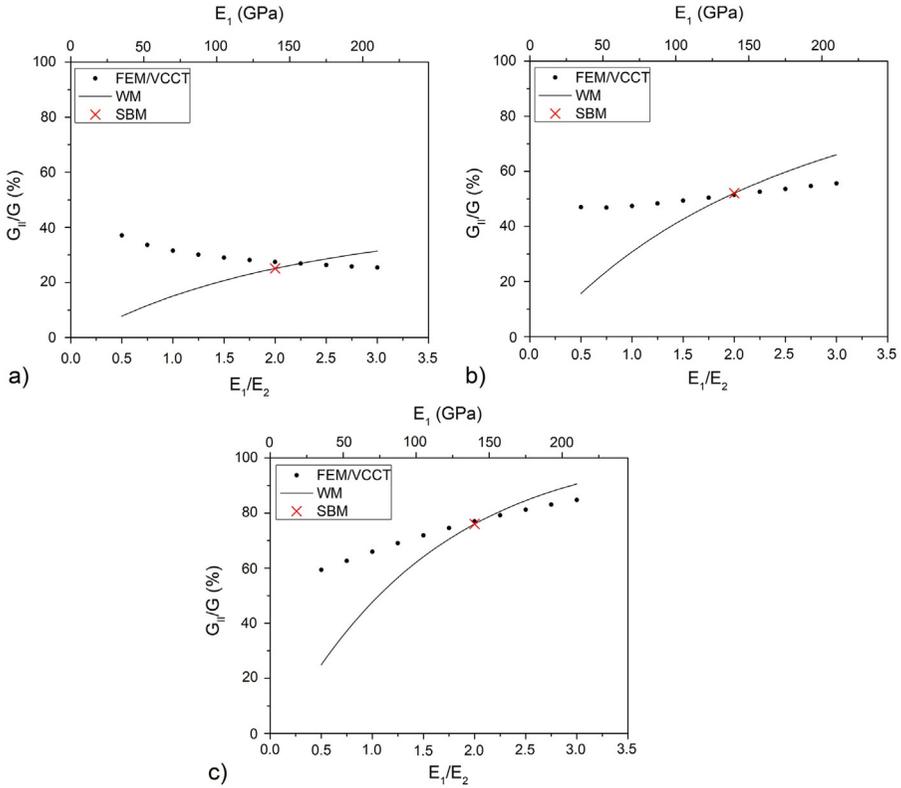
Fig. 17.10 Fracture mode ratio with the variation of specimen material: cases (a) 4—low, (b) 5—intermediate, and (c) 6—high mode II [27].
Reprinted with permission from Taylor & Francis Ltd, http://www.tandfonline.com.

Table 17.4 Results and errors of the analytical model in the condition of strain equivalence.

	Numerical model		Strain-based method (SBM)			
Case	G (J/m^2)	G_{II}/G (%)	G (J/m^2)	Error (%)	G_{II}/G (%)	Error (%)
4	306.0	27.5	309.0	1.0	25.1	−8.6
5	84.2	51.5	77.4	−8.1	52.1	1.1
6	41.3	77.0	40.5	−2.0	76.0	−1.3

Table 17.5 Mechanical properties of the materials.

Material	Elastic modulus, E_{11} (GPa)	Poisson's ratio, ν_{12}
Steel	200	0.27
Composite 0/90	46	0.24
Adhesive	2.25	0.38

Table 17.6 Test matrix.

Test	Specimen	Metal arm thickness, h_1 (mm)	Composite arm thickness, h_2 (mm)	Lever length, c (mm)	Lever center of gravity, c_g (mm)	Lever weight, P_g (kg)
1	Thick	6.35	13.35	78	31	17.6
2	Thick	6.35	13.35	78	31	17.6
3	Thin	3.18	6.34	110	40	17.6
4	Thin	3.18	6.34	110	40	17.6

an error of 27.8% in the first measurement of crack propagation and this reduces as the crack length increases, down to 11.4% in the last propagation point. The fracture mode ratio (G_{II}/G) presented nearly constant values of 23.5% in the SBM and 21.5% in the FEM, as observed in Fig. 17.11c. A constant fracture mode ratio is expected from the MMB test. The total fracture energy of Tests 3 and 4, in thin specimens, are presented in Fig. 17.12a and b, respectively. In this geometry, the SBM produced an error of 13.2% in the first measurement of crack propagation and this reduced as the crack length increases, down to 2.6% in the last propagation point. The analytical method produced more accurate results in the thin specimens compared to the thick ones. Moreover, the analytical solution showed more accuracy as the crack length increases due to the reduction of transverse shear effect that is not considered in the analytical
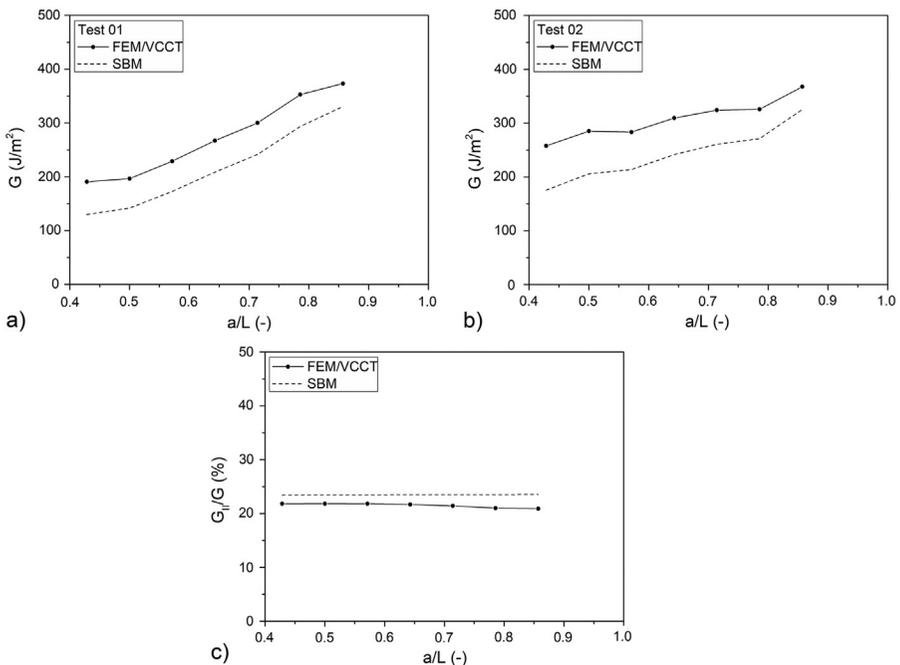

Fig. 17.11 Total fracture energy and mode ratio of thick specimens [27]. Reprinted with permission from Taylor & Francis Ltd, http://www.tandfonline.com.
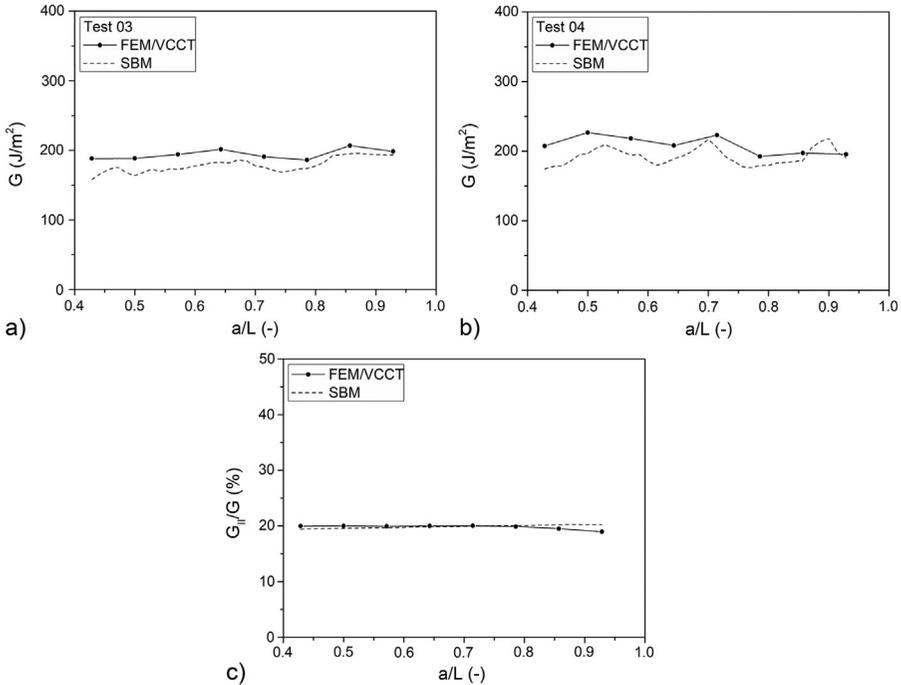
Fig. 17.12 Total fracture energy and mode ratio of thin specimens [27].
Reprinted with permission from Taylor & Francis Ltd, http://www.tandfonline.com.

model but can be significant in a specimen with relatively large thickness. Finally, thin specimens presented a nearly constant fracture mode ratio (G_{II}/G) of 19.8% from both the SBM and the FEM, as shown in Fig. 17.12c. This shows the accuracy of the analytical solution and agrees with the results obtained from the parametric study in the previous section. Overall, the SBM gives reliable results for the calculation of the total fracture energy and mode ratio of cracks at a bi-material interface as long as the shear effects are negligible.

17.5 Mixed-mode fracture behavior

17.5.1 Crack stability

Crack stability is an important issue in the fracture testing of adhesively bonded joints, as only for stable cracking can the change in applied force (and hence the compliance) be measured for a growing crack. A crack is unstable if an infinitesimal change in displacement is accompanied by a finite change in the crack length. The stability of crack growth may be judged from the sign of dG/da. Stable crack growth occurs if:

$$\frac{dG}{da} \leq 0 \tag{17.28}$$

The energy release rate was defined as the Irwin-Kies equation [8]:

$$G = \frac{P^2}{2b} \frac{dC}{da} \qquad (17.29)$$

where P is the applied load and C is the compliance defined by δ/P (δ is the displacement) and b is the specimen width. In this form, linear elastic behavior is assumed and in the following, G_c is assumed to be independent of rate. Considering the crack propagates very quickly with the displacement increment, the loading process is analogous to a condition of fixed grips. Eq. (17.29) can be transformed as:

$$G = \frac{\delta^2}{2bC^2} \frac{dC}{da} \qquad (17.30)$$

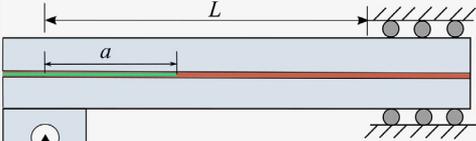Combing Eqs. (17.28) and (17.30) leads to the stability criterion for fracture tests [23]:

$$\frac{1}{2} C \frac{d^2 C}{da^2} \frac{1}{(dC/da)^2} \leq 1 \qquad (17.31)$$

Based on this theory, the stability criteria for a variety of fracture tests have been successfully derived, as documented in Table 17.7. Specimen precracking is always recommended prior to a fracture test, as unstable crack growth can occur when testing the specimen directly from an insert. The resistance to crack initiation from an inserted release film (positioned in the adhesive layer during manufacture of the joint) may impose a greater initial crack resistance with $(dG/da) > 0$. Precracking the specimen so that the crack length can extend by a short distance from its initial length can improve stability.

However, unstable fracture behavior can still occur despite the initial crack length satisfying the above criteria, as crack stability is highly dependent upon the adhesive properties. An unstable fracture is more likely to occur in joints bonded with a brittle adhesive while joints bonded with a tougher adhesive tend to result in stable fracture behavior [47]. Moreover, crack stability is very sensitive to the mixed-mode ratio. While stable fracture can be obtained in the adhesively bonded CFRP under mode I and mode II loadings, an unstable crack may appear in the mixed mode I/II loading. Researchers, such as [48], also reported that the crack in glass epoxy laminates bonded with Redux 420 epoxy adhesive propagated very rapidly and unstably under mode I dominated loading, whereas the propagation became more stable under mode II dominated loading, when the fracture resistance was greater.

The fracture behavior of asymmetric specimens suggests that the size of the cohesive zone may be a critical factor governing the stability of crack growth in adhesive joints [46]. In the AFRMM joints loaded via the thinner arm (mode I dominated), the crack was found to grow stably within the adhesive. In contrast, in the case loaded with the thicker arm (mode II dominated), the response became rather unstable with the crack propagating to the clamping point abruptly, associated with a change in the type of failure from cohesive in the adhesive layer to interlaminar in the CFRP substrates.
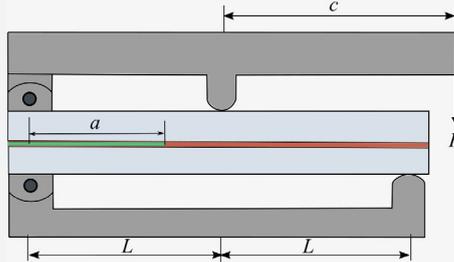
Table 17.7 Specimen configuration and stability criteria for fracture testing of laminated composites and adhesive joints loaded in displacement control.

Fracture tests	Specimen configurations	Stability criteria	References
DCB and ADCB		Always stable	[32]
ELS		$a/L \geq 0.56$	[32]
3ENF		$a/L \geq 0.68$	[32]
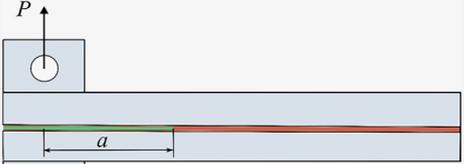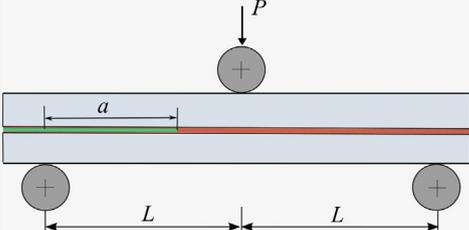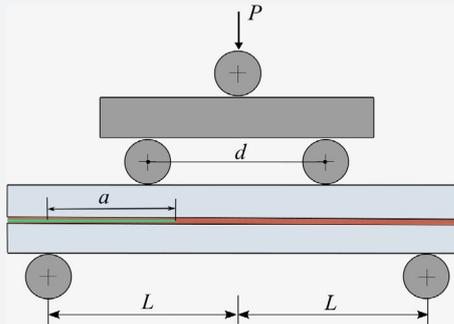
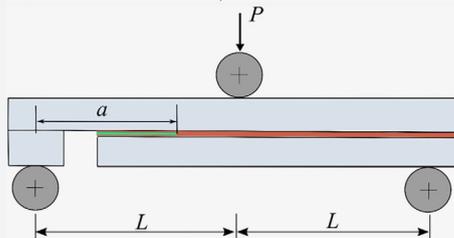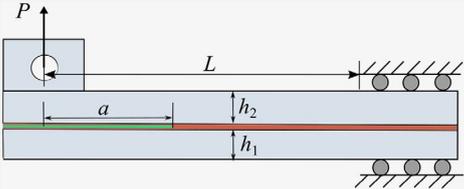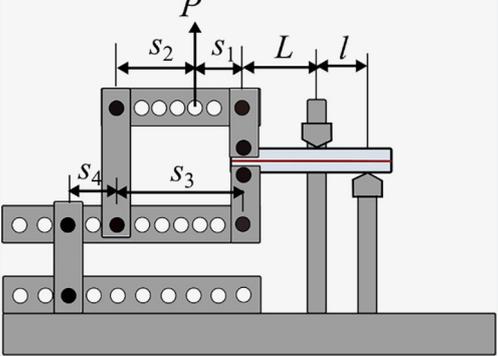| 4ENF | | Always stable. Enough space between the loading pin and the crack tip should be allowed to rule out any unwanted effects from the compressive stresses of the loading pin. | [43] |
| MMB | | $a/L \geq \left[\dfrac{(c+L)^2}{4(3c-L)^2 + 3(c+L)^2} \right]^{\frac{1}{3}}$ | [44] |
| MMF (or SLB) | | $a/L \geq 0.49$ | [45] |

Table 17.7 Continued

Fracture tests	Specimen configurations	Stability criteria	References
FRMM ($h_1 = h_2$)		$a/L \geq 0.41$	[32]
AFRMM ($h_1 \neq h_2$)		$a/L \geq \frac{\alpha}{1+\alpha} \left[\frac{(1+\alpha)^2 (1+\alpha^3)}{2((1+\alpha)^2 + 3\alpha^4)} \right]^{\frac{1}{3}}$ $\alpha = \frac{h_2}{h_1} = \frac{\text{Loaded arm}}{\text{Unloaded arm}}$	[46]
SPELT		$a/L \geq \left[\frac{1 + l/L}{1 + \beta^*(\psi)} \right]^{\frac{1}{3}}$ ψ is the nominal phase angle of loading, and $\beta^*(\psi)$ is the dimensionless geometry parameter	[15]

The FEA simulation suggests extensive damage accumulated ahead of the crack tip in the AFRMM specimen loaded via the thicker arm, leading to much longer cohesive zones than those loaded inversely. In addition, the length of the cohesive zone decreased rapidly after reaching a maximum. This abrupt reduction could explain the unstable nature of these tests (Fig. 17.13).
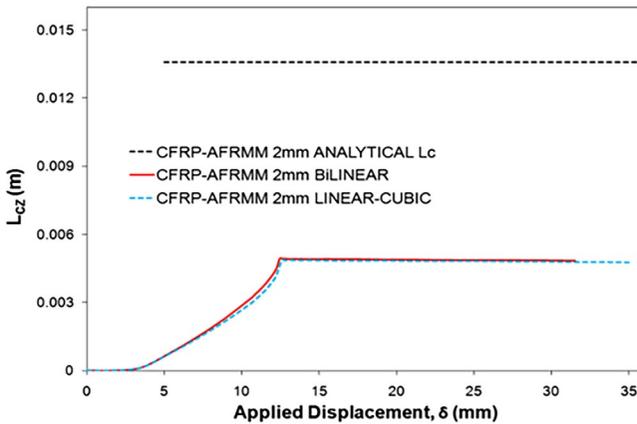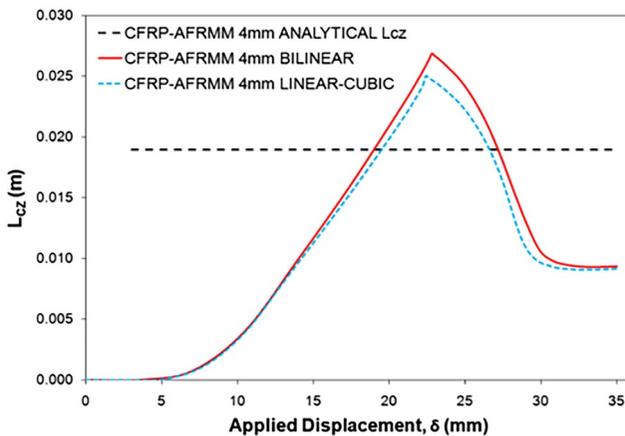
Fig. 17.13 The cohesive zone length as a function of applied displacement in AFRMM specimens loaded at (a) the thinnest and (b) the thickest arms from FEA simulations, assuming a bilinear and a linear cubic traction separation law, and from an analytical method. The analytical estimate was calculated by adding the contributions of the pure mode components of G_{IC}^m and G_{IIC}^m, that is, $l_{CZ}^m = l_{CZ,\ I}(G_{IC}^m) + l_{CZ,\ II}(G_{IIC}^m)$ [46].

17.5.2   Crack paths

Crack path is a major concern for the fracture analysis of layered materials. Due to the existence of elastic mismatch, microdefects, and residual stresses on the interface, it is quite challenging to predict the crack paths analytically. Fleck et al. [49] established LEFM theories to predict the crack path in adhesively bonded structures under mode I with finite mode II loading, based on the experimentally established fact that a crack advancing continuously in an isotropic, homogeneous, brittle solid selects a trajectory where local stress intensity factor $K_{II} = 0$. The remote field in the asymptotic problem in Fig. 17.14 is specified by K_I^∞, K_{II}^∞, T^∞, and σ^0, where K_I^∞ and K_{II}^∞ are the remote values of the mode I and mode II stress intensity factors, respectively; T^∞ is the remote T-stress; and σ^0 is the σ_{xx} component of residual stress preexisting in the adhesive due to thermal mismatch or other sources. The solution to the elasticity problem (as shown in Fig. 17.14) provides the local K_I, K_{II}, and T at the crack tip within the layer, and is given by the following equations, with c_I and c_{II} and $\phi_H(\alpha,\beta) + \omega(\alpha,\beta)$ being tabulated in [49].

Note that the parameter β used in this section has a different definition to β defined elsewhere in the chapter. The local (K_I, K_{II}) depends only on the remote loads K_I^∞ and K_{II}^∞, and the two sets are connected by the energy release rate due to conservation of the J-integral:

$$K_I + iK_{II} = \left(\frac{1-\alpha}{1+\alpha}\right)^{1/2}\left(K_I^\infty + K_{II}^\infty\right)e^{i\phi} \tag{17.32}$$
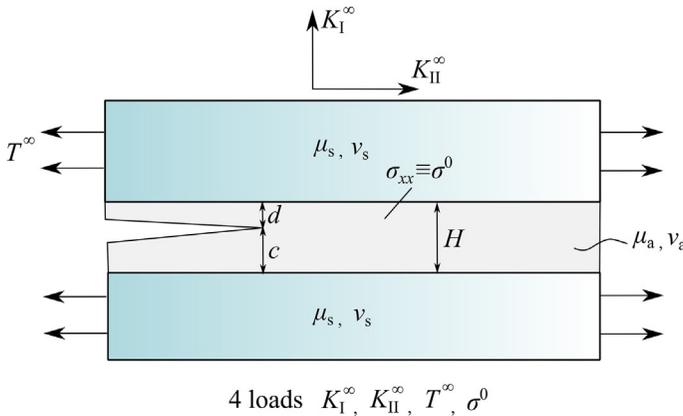

Fig. 17.14 The elasticity problem.
Redrawn after N.A. Fleck, J.W. Hutchinson, Z. Suo, Crack path selection in a brittle adhesive layer, Int. J. Solids Struct. 27 (1991) 1683–703.

where ϕ can be interpreted as a phase angle shift between the remote and local stress intensities, $\phi \equiv \tan^{-1}(K_{II}/K_I) - \tan^{-1}(K_{II}^\infty/K_I^\infty)$. ϕ is only a function of structures, that is, $\phi = \phi(c/H, \alpha, \beta)$:

$$\phi = \varepsilon \ln\left(\frac{H-c}{c}\right) + 2\left(\frac{c}{H} - \frac{1}{2}\right)[\phi_H(\alpha, \beta) + \omega(\alpha, \beta)] \qquad (17.33)$$

where α, β are Dundurs elastic mismatch parameters, $\varepsilon = (1/2\pi)\ln[(1-\beta)/(1+\beta)]$, c/H is the crack location as illustrated in Fig. 17.14, the function $\omega(\alpha, \beta)$ is tabulated in [50] and ϕ_H is given in Hutchinson et al. [51].

The local T-stress depends linearly on all four loading parameters.

$$T = \frac{1-\alpha}{1+\alpha}T^\infty + \sigma^0 + c_I \frac{K_I^\infty}{\sqrt{H}} + c_{II}\frac{K_{II}^\infty}{\sqrt{H}} \qquad (17.34)$$

where the two nondimensional functions, $c_I(c/H, \alpha, \beta)$ and $c_{II}(c/H, \alpha, \beta)$, are given in [49].

A necessary condition for the existence of a straight path within the layer is the location of a path with $K_{II} = 0$. Such a path will only be stable if $T < 0$. Symmetry indicates that a crack along the center line of a layer joining identical materials and subject to remote pure mode I loading will be under pure mode I locally. When the base specimen carries some mode II in addition to mode I, the crack may find a pure mode I path off the center line. When the mode II component is sufficiently large, typically $\tan^{-1}(K_{II}^\infty/K_I^\infty) \geq 15$ degrees, the crack runs along the adhesive/substrate interface and the measured G_c is the mode-dependent interfacial fracture energy. For values of K_{II}^∞/K_I^∞ outside the range of possible retention of the crack within the layer (such as, $\tan^{-1}(K_{II}^\infty/K_I^\infty)$ greater than 0–10 degrees depending on the mismatch), the crack will be driven toward one interface or the other—toward the lower interface if $K_{II}^\infty > 0$ and toward the upper if $K_{II}^\infty < 0$ [52].

For tough adhesive systems in which LEFM may not still be valid, there exists considerable experimental evidence that suggests that the type of loading affects the crack propagation path (i.e., loci of failure). Mixed mode I/II tends to drive the crack toward the interface of the adhesive joint. For instance, Blackman et al. [53] reported that the adhesively bonded CFRP joints loaded in mixed-mode ($G_I/G_{II} = 4/3$) failed via a delamination mechanism, with the crack switching from the position of the cohesive precrack to a path within the composite substrate, in contrast to the cohesive failure that occurred under the pure mode I or mode II loading. Blackman et al. pointed out that this type of failure was related to the transverse tensile stresses (σ_{yy}) exerted on the CFRP substrates. If the transverse stresses exceeded the transverse strength (σ_{yyc}), fracture could take place in the composite arms. An approximation to the transverse stress, σ_{yy}, on a single substrate for the loading modes was developed that indicated that the greatest transverse stresses were produced by mixed-mode loading using the FRMM specimen, which has only a single arm being loaded.

17.5.3 Failure envelopes

A comprehensive review of failure envelopes, including information on the type of responses modeled in each case, can be found in [54]. These criteria were initially developed for composite materials, but there is much evidence showing they are also valid for adhesive joints. The most widely used empirical criteria for the failure of adhesive joints are the power criterion [55] (Eq. 17.35) and the B-K criterion [42] (Eq. 17.36). Both criteria were implemented in several commercial finite element analysis codes.

$$\left(\frac{G_{\mathrm{I}}}{G_{\mathrm{Ic}}}\right)^{m} + \left(\frac{G_{\mathrm{II}}}{G_{\mathrm{IIc}}}\right)^{n} = 1 \tag{17.35}$$

$$G_{\mathrm{I/IIc}} = G_{\mathrm{Ic}} + (G_{\mathrm{IIc}} - G_{\mathrm{Ic}})\left(\frac{G_{\mathrm{II}}}{G_{\mathrm{I}} + G_{\mathrm{II}}}\right)^{\eta} \tag{17.36}$$

Fig. 17.15 presents the fracture toughness as a function of the mode-mixity (G_{II}/G) for the unidirectionally reinforced carbon fiber composite substrates bonded with the epoxy adhesive, 3M-D460 [56]. The power law captured the failure envelope of the adhesive joints when the exponents $m=0.63$ and $n=1.43$, and indeed the power law criterion with a single exponent of 1.0 has been able to provide a satisfactory fit.

It has been reported that the B-K failure criterion successfully described the failure behavior of adhesive joints employing metallic substrates. Fig. 17.16 shows the fracture toughness of the crash-resistant epoxy adhesive SikaPowers-498 measured under various values of mixed-mode ratio using TDCB and MMB tests [57]. Fig. 17.17 gives another example of the fracture toughness of Araldite-2015 bonded metallic joints determined by DCB and MMB tests [58]. For both sets of experimental data, there was a steady increase in the fracture resistance as the mixed-mode ratio increased from 0 (pure mode I) to 1 (pure mode II). The B-K model captured the fracture behavior as a function of mixed-mode ratio closely.
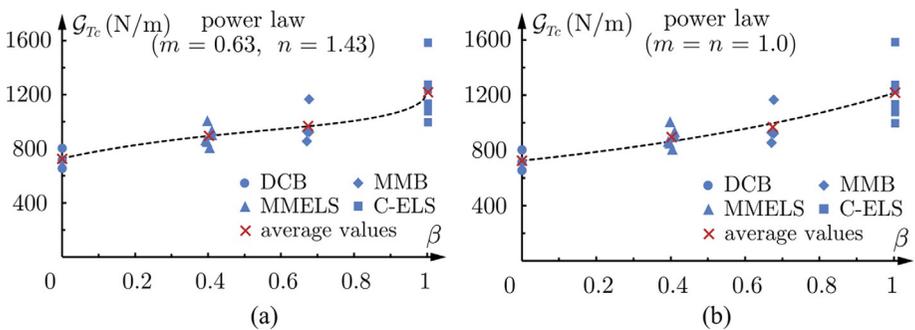

Fig. 17.15 Values of G-total (G_{Tc}) as a function of mixed-mode ratio $\beta = G_{\mathrm{II}}/G_{\mathrm{Tc}}$ for: (a) exponents $m=0.63$ and $n=1.43$ and (b) a single exponent of 1.0 [56].
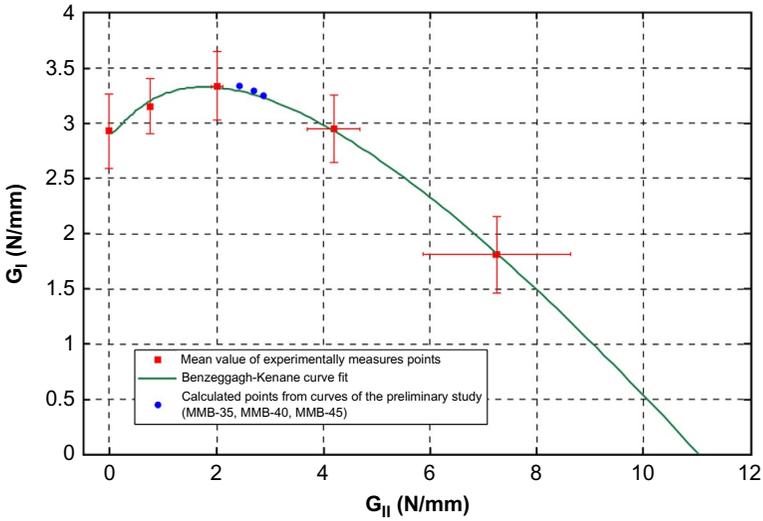
Fig. 17.16 Mixed-mode fracture data measured on joints employing metallic substrates bonded with SikaPower 498 adhesive, fitted using the B-K criterion [57].
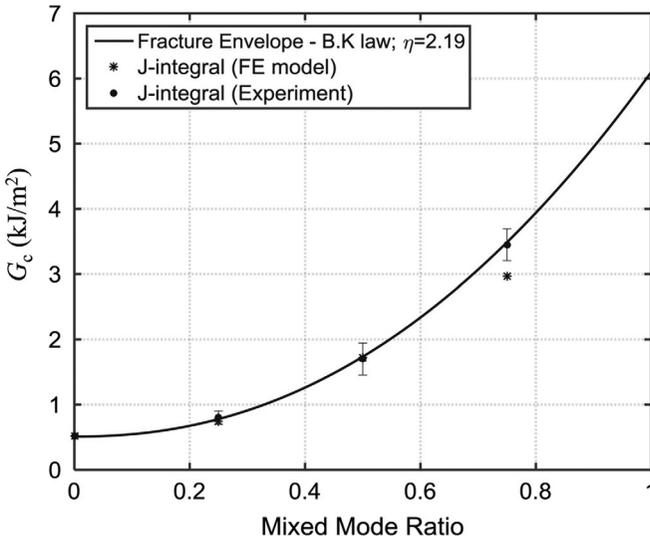

Fig. 17.17 Mixed-mode fracture data measured on joints employing metallic substrates bonded with Araldite 2015 adhesive, fitted using the B-K criterion [58].
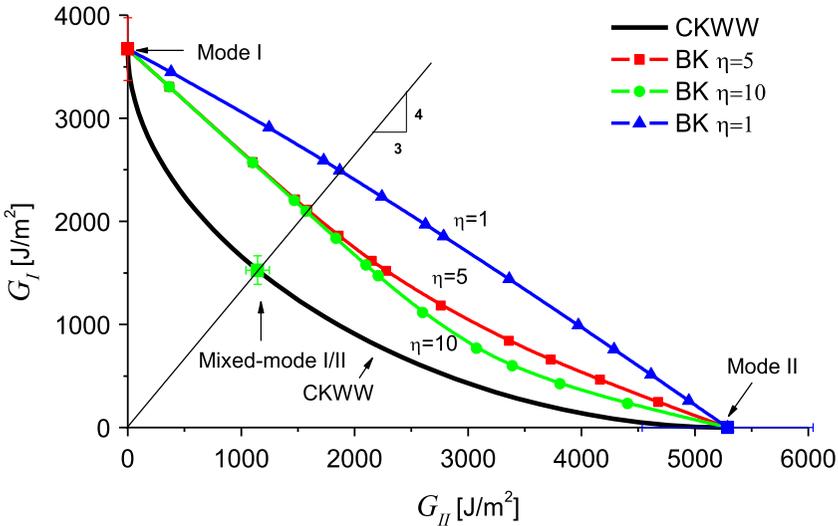
Fig. 17.18 Comparison of the use of the CKWW and BK criteria for construction of the failure envelope for joints bonded with a toughened automotive adhesive XD4600, when substrate delamination occurred [59].

The B-K model requires that the fracture toughness value always increases as the contribution of mode II is increased, that is, $G_{Ic} < G_{I/IIc} < G_{IIc}$; however, such a monotonically increasing trend is not always measured for adhesive joints. Fig. 17.18 presents B-K criteria constructed for joints bonded with the toughened automotive adhesive XD4600 under quasistatic loading [59]. Different values of η were used for the B-K criterion, but it was not possible for this model to fit the low mixed-mode I/II values produced when a switch in crack propagation path to interfacial failure or composite delamination occurred. Clearly, these joints that showed substrate delamination under mixed-mode loading did not comply with the "monotonic increase" requirement. Similar nonmonotonic behavior caused by the failure mechanism changing from cohesive (in the adhesive) to adhesive (on the carrier cloth/adhesive interface) under the mixed-mode loading was also reported by Dillard et al. [60]. However, the Charalambides, Kinloch, Wang, and Williams (CKWW) criterion [61] (in Eq. (17.37)) was found to be capable of capturing the nonmonotonic fracture envelope due to the criterion having two fitting parameters, κ and φ, which enabled the fitting of more complex failure envelopes.

$$\left(\frac{G_I}{G_{Ic}} - 1\right)\left(\frac{G_{II}}{G_{IIc}} - 1\right) - \left[\kappa + \varphi\left(\frac{G_I}{G_I + G_{II}}\right)\right]\left(\frac{G_I}{G_{Ic}}\right)\left(\frac{G_{II}}{G_{IIc}}\right) = 0 \qquad (17.37)$$

Fig. 17.19 displays another example of fitting failure envelopes [62]. The fracture toughness determined at the point of the maximum load, in which the discrete value for $\beta = 0.25$ violates a monotonic trend, that is, in the range of $\beta < 0.25$ the G_c decreases with increasing mixity but when $\beta > 0.25$ it increases. The B-K criterion
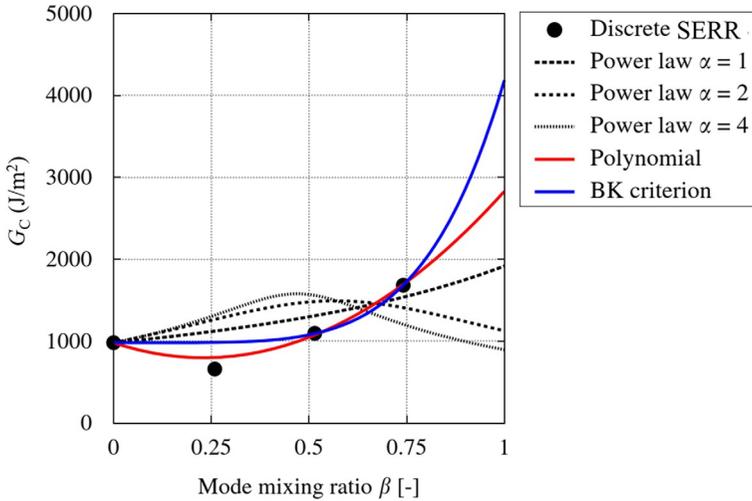
Fig. 17.19 Comparison of the use of the various failure criteria for construction of the failure envelopes for unidirectional Hexcel IM7/8552 carbon/epoxy composite bonded with film adhesive Cytec FM 300 M [62].

and the power law with $\alpha_1 = \alpha_2 = 1$, both of which require a monotonical increase in G_c values, did not yield good approximation of the G_c value at $\beta = 0.25$. Instead, the best fit of the G_c values is obtained by the second order polynomial, clearly capturing the transition in the G_c value at $\beta = 0.25$.

17.6 Conclusions and outlook

The characterization of fracture in adhesively bonded joints under mixed-mode (I/II) loading conditions has been discussed. While standardized tests for adhesive joints in mixed-mode are not yet available, much use has been made of methods developed initially for composite laminates such as the mixed-mode bend test, the fixed-ratio mixed-mode test with both symmetric and asymmetric geometry, and the asymmetric double cantilever beam. Most analyses utilize LEFM and corrected beam theory to determine the fracture resistance as a function of mixed-mode ratio.

Efforts to partition the mixed-mode (I/II) fracture resistance into pure mode components have typically followed either a local singular field approach or a global approach. The application of these partitioning strategies to adhesively bonded joints has led to the conclusion that neither strategy works well across the wide spectrum of adhesives in common usage. The local singular field approach has been shown to be more suitable when brittle adhesives are employed (when the damage zone ahead of the crack tip is very limited in size.) Conversely, the global partitioning approach is shown to be more suitable when toughened adhesives are employed (when the damage zone ahead of the crack tip is larger.) A semianalytical cohesive zone analysis has been shown to work equally well across the wide spectrum of adhesives in use. This

approach utilizes a singularity factor that scales from the local to the global solutions and therefore has wide applicability.

The limitations of global partitioning have been further explored with the goal to design and analyze adhesive joints with dissimilar adherends—a bi-material interface joint. The definition of mode I loading in the mixed-mode case has been modified by the incorporation of a longitudinal strain criteria. Further, the coupling between mode I and II components and their contribution to the total mixed-mode fracture energy has been considered and the technique has been verified numerically. Such an approach offers advantages for the design of adhesive joints with dissimilar adherends and their analysis.

Finally, the issues of crack stability, crack path selection, and failure envelopes for mixed-mode loading were considered.

In terms of future trends, as adhesives become more highly toughened they present larger damage zones at the crack tip and the use of LEFM becomes increasingly inaccurate. As such, nonlinear methods such as the *J*-integral (also described in Chapter 16), and the adaptation of the inclinometer test methods to mixed-mode testing will increasingly be required. Also, developments in experimental techniques such as digital image correlation, which can be used to simultaneously track the crack growth, measure the traction-separation law, and determine J_c, will become more popular [47,63]. Also, as materials become more complex, especially layered or laminated materials that can be incorporated into adhesively bonded joints, then there is significant scope to design more fracture-resistant systems where knowledge of the failure paths under mixed-mode loading can be exploited.

References

[1] A.J. Kinloch, Adhesion and Adhesives: Science and Technology, Chapman & Hall, London, 1987.

[2] L.F.M. Da Silva, A. Öchsner, R.D. Adams, Handbook of Adhesion Technology, Springer-Verlag Berlin Heidelberg, Heidelberg, 2011.

[3] E.J. Ripling, S. Mostovoy, R.L. Patrick, Measuring fracture toughness of adhesive joints, Mater. Res. Stand. 4 (1964) 129–134.

[4] ASTM D3433-93, Standard Test Method for Fracture Strength in Cleavage of Adhesives in Bonded Metal Joints, 1993.

[5] K.M. Liechti, T. Freda, On the use of laminated beams for the determination of pure and mixed-mode fracture properties of structural adhesives, J. Adhes. 28 (1989) 145–169.

[6] S. Li, J. Wang, M.D. Thouless, The effects of shear on delamination in layered materials, J. Mech. Phys. Solids 52 (2004) 193–214.

[7] H.K. Singh, A. Chakraborty, C.E. Frazier, D.A. Dillard, Mixed mode fracture testing of adhesively bonded wood specimens using a dual actuator load frame, Holzforschung 64 (2010) 353–361.

[8] G.R. Irwin, J.A. Kies, Critical energy release rate analysis of fracture strength of large welded structures, Weld. J. 33 (1954) 193–198.

[9] Chaves F.J.P., Silva L.F.M., De Moura M.F.S.F., Dillard D.A., Esteves C., Chaves F.J.P., et al. Fracture mechanics tests in adhesively bonded joints: a literature review J. Adhes. 90 2014; 8464.F.J.P. Chaves, L.F.M. Silva, M.F.S.F. De Moura, D.A. Dillard, C. Esteves, F.J.

P. Chaves, et al., Fracture mechanics tests in adhesively bonded joints: a literature review, J. Adhes. 90 (2014) 955–992.

[10] B.F. Sørensen, P. Brethe, P. Skov-Hansen, Controlled crack growth in ceramics: the DCB specimen loaded with pure moments, J. Eur. Ceram. Soc. 16 (1996) 1021–1025.

[11] L.A. Carlsson, J.W. Gillespie, R.B. Pipes, On the Analysis and Design of the End Notched Flexure (ENF) Specimen for Mode II Testing, J. Compos. Mater. 20 (1986) 594–604.

[12] B.R.K. Blackman, A.J. Kinloch, M. Paraschi, The determination of the mode II adhesive fracture resistance, G_{IIC}, of structural adhesive joints: an effective crack length approach, Eng. Fract. Mech. 72 (2005) 877–897.

[13] J.R. Reeder, J.H. Crews, Nonlinear analysis and redesign of the Mixed-Mode bending Delamination test, Langley Research Center Hampton, Virginia, 1991.

[14] M. Arcan, Z. Hashin, A. Voloshin, A method to produce uniform plane-stress states with applications to fiber-reinforced materials - a specially designed specimen yields material properties under pure shear or uniform plane-stress conditions, Exp. Mech. 18 (1978) 141–146.

[15] G. Fernlund, J.K. Spelt, Mixed-mode fracture characterization of adhesive joints, Compos. Sci. Technol. 50 (1994) 441–449.

[16] ASTM: D6671M, Standard Test Method for Mixed Mode I-Mode II Interlaminar Fracture Toughness of Unidirectional Fiber Reinforced Polymer Matrix Composites, 2006.

[17] M. Costa, R. Carbas, E. Marques, G. Viana, L.F.M. da Silva, An apparatus for mixed-mode fracture characterization of adhesive joints, Theor. Appl. Fract. Mech. 91 (2017) 94–102.

[18] Y.H. Lai, M.D. Rakestraw, D.A. Dillard, The cracked lap shear specimen revisited - a closed form solution, Int. J. Solids Struct. 33 (1996) 1725–1743.

[19] W.S. Johnson, Stress analysis of the cracked-lap-shear specimen - an ASTM round-robin, J. Test. Eval. 15 (1987) 303–324.

[20] E. Panettieri, G. Leclerc, J. Jumel, J. Guitard, Mixed-mode crack propagation tests of composite bonded joints using a dual-actuator load frame_Constant and variable GII/G conditions, Eng. Fract. Mech. 202 (2018) 471–486.

[21] T. Yang, V. Gandhi, R. Huang, K.M. Liechti, Rate dependent fracture along a silicone / epoxy interface under mixed-mode loading conditions, Int. J. Solids Struct. (2022) (in press).

[22] J.G. Williams, The fracture mechanics of delamination tests, J. Strain Anal. Eng. Des. 24 (1989) 207–214.

[23] J.G. Williams, On the calculation of energy release rates for cracked laminates, Int. J. Fract. 36 (1988) 101–119.

[24] M. Conroy, A.J. Kinloch, J.G. Williams, A. Ivankovic, Mixed mode partitioning of beam-like geometries: a damage dependent solution, Eng. Fract. Mech. 149 (2015) 351–367.

[25] D. Álvarez, F.J. Guild, A.J. Kinloch, B.R.K. Blackman, Partitioning of mixed-mode fracture in adhesively-bonded joints: experimental studies, Eng. Fract. Mech. 203 (2018) 224–239.

[26] B.D. Davidson, S.J. Gharibian, L. Yu, Evaluation of energy release rate-based approaches for predicting delamination growth in laminated composites, Int. J. Fract. 105 (2000) 343–365.

[27] M.M. Arouche, S. Teixeira de Freitas, S. de Barros, Evaluation of the strain-based partitioning method for mixed-mode I+II fracture of bi-material cracks, J. Adhes. 98 (2022) 577–605.

[28] J.G. Williams, Large displacement and end block effects in the "DCB" interlaminar test in Modes I and II, J. Compos. Mater. 21 (1987) 330–347.

[29] J.G. Williams, End corrections for orthotropic DCB specimens, Compos. Sci. Technol. 35 (1989) 367–376.

[30] M.F. Kanninen, A dynamic analysis of unstable crack propagation and arrest in the DCB test specimen, Int. J. Fract. 10 (1974) 415–430.

[31] Y. Wang, J.G. Williams, Corrections for mode II fracture toughness specimens of composites materials, Compos. Sci. Technol. 43 (1992) 251–256.

[32] S. Hashemi, A.J. Kinloch, J.G. Williams, The analysis of interlaminar fracture in uniaxial fibre-polymer composites, Proc. R. Soc. Lond. A 427 (1990) 173–199.

[33] F. Ducept, P. Davies, D. Gamby, An experimental study to validate tests used to determine mixed mode failure criteria of glass/epoxy composites, Compos. A: Appl. Sci. Manuf. 28 (1997) 719–729.

[34] F. Ducept, D. Gamby, P. Davies, A mixed-mode failure criterion derived from tests on symmetric and asymmetric specimens, Compos. Sci. Technol. 59 (1999) 609–619.

[35] M.M. Arouche, W. Wang, S. Teixeira de Freitas, S. de Barros, Strain-based methodology for mixed-mode I+II fracture: a new partitioning method for bi-material adhesively bonded joints, J. Adhes. 95 (2019) 385–404.

[36] Z. Ouyang, G. Ji, G. Li, On approximately realizing and characterizing pure mode-I interface fracture between bonded dissimilar materials, J. Appl. Mech. 78 (2011) 1–12.

[37] W. Wang, R. Lopes Fernandes, S. Teixeira De Freitas, D. Zarouchas, R. Benedictus, How pure mode I can be obtained in bi-material bonded DCB joints: a longitudinal strain-based criterion, Compos. Part B Eng. 153 (2018) 137–148.

[38] V. Mollón, J. Bonhomme, A. Argüelles, J. Viña, Influence of the crack plane asymmetry over G II results in carbon epoxy ENF specimens, Compos. Struct. 94 (2012) 1187–1191.

[39] J.R. Reeder, J.H. Crews, Redesign of the mixed-mode bending delamination test to reduce nonlinear effects, J. Compos. Technol. Res. 14 (1992) 12–19.

[40] J.R. Reeder, A bilinear failure criterion for mixed-mode delamination, in: Composite Materials: Testing and Design, ASTM STP 1206, vol. 11, American Society for Testing and Materials, Philadelphia, 1993, pp. 302–322.

[41] J.H. Chen, R. Sernow, E. Schulz, G. Hinrichsen, Modification of the mixed-mode bending test apparatus, Compos. A: Appl. Sci. Manuf. 30 (1999) 871–877.

[42] M.L. Benzeggagh, M. Kenane, Measurement of mixed-mode delamination fracture toughness of unidirectional glass/epoxy composites with mixed-mode bending apparatus, Compos. Sci. Technol. 56 (1996) 439–449.

[43] C. Schuecker, B.D. Davidson, Evaluation of the accuracy of the four-point bend endnotched flexure test for mode II delamination toughness determination, Compos. Sci. Technol. 60 (2000) 2137–2146.

[44] Y.J. Yum, A.H. You, Pure mode I, II and mixed mode interlaminar fracture of graphite/ epoxy composite materials, J. Reinf. Plast. Compos. 20 (2001) 794–808.

[45] A. Szekrényes, Crack stability of fracture specimens used to test unidirectional fiber reinforced material, Exp. Mech. 50 (2010) 473–482.

[46] D. Alvarez Feito, Fracture mechanics of carbon fibre reinforced plastics to Ti-alloy adhesive joints (Ph.D. thesis), Imperial College London, 2012.

[47] F. Sun, B.R.K. Blackman, A DIC method to determine the Mode I energy release rate G, the J-integral and the traction-separation law simultaneously for adhesive joints, Eng. Fract. Mech. 234 (2020), 107097.

[48] F. Ducept, P. Davies, D. Gamby, Mixed mode failure criteria for a glass/epoxy composite and an adhesively bonded composite/composite joint, Int. J. Adhes. Adhes. 20 (2000) 233–244.

[49] N.A. Fleck, J.W. Hutchinson, Z. Suo, Crack path selection in a brittle adhesive layer, Int. J. Solids Struct. 27 (1991) 1683–1703.

[50] R. Huang, Z. Suo, J.H. Prevost, W.D. Nix, Inhomogeneous deformation in metallic glasses, J. Mech. Phys. Solids 50 (2002) 1011–1027.

[51] J.W. Hutchinson, M.E. Mear, J.R. Rice, Crack paralleling an interface between dissimilar materials, J. Appl. Mech. 54 (1987) 828–832.

[52] J.W. Hutchinson, Z. Suo, Mixed mode cracking in layered materials, Adv. Appl. Mech. 29 (1991) 63–191.

[53] B.R.K. Blackman, A.J. Kinloch, F.S. Rodriguez-Sanchez, W.S. Teo, The fracture behaviour of adhesively-bonded composite joints: effects of rate of test and mode of loading, Int. J. Solids Struct. 49 (2012) 1434–1452.

[54] J.R. Reeder, 3-D mixed mode delamination fracture criteria - an Experimentalist's perspective, in: B. Sankar, A. Waas, M. Hyer (Eds.), Damage in Composites, Destech Publications, Lancaster, PA, 2013, pp. 129–146.

[55] E.M. Wu, R.C. Reuter, Crack Extension in Fiberglass Reinforced Plastics, Report No. 275, University of Illinois, Urbana, IL, 1965.

[56] I. Simon, L. Banks-Sills, Mixed mode I/II interlaminar initiation fracture toughness of a secondary bonded pultrusion composite laminate, Theor. Appl. Fract. Mech. 114 (2021), 103018.

[57] G. Stamoulis, N. Carrere, J.Y. Cognard, P. Davies, C. Badulescu, On the experimental mixed-mode failure of adhesively bonded metallic joints, Int. J. Adhes. Adhes. 51 (2014) 148–158.

[58] M.Z. Sadeghi, J. Zimmermann, A. Gabener, K.U. Schroeder, The applicability of J-integral approach in the determination of mixed-mode fracture energy in a ductile adhesive, Int. J. Adhes. Adhes. 83 (2018) 2–8.

[59] F.S. Rodriguez-Sanchez, Fracture Behaviour of Automotive Adhesive Joints, Imperial College London, 2008 (Ph.D. thesis).

[60] D.A. Dillard, H.K. Singh, D.J. Pohlit, J.M. Starbuck, Observations of decreased fracture toughness for mixed mode fracture testing of adhesively bonded joints, J. Adhes. Sci. Technol. 23 (2009) 1515–1530.

[61] M. Charalambides, A.J. Kinloch, Y. Wang, J.G. Williams, On the analysis of mixed-mode failure, Int. J. Fract. 54 (1992) 269–291.

[62] C. Balzani, W. Wagner, D. Wilckens, R. Degenhardt, S. Büsing, H.G. Reimerdes, Adhesive joints in composite laminates - A combined numerical/experimental estimate of critical energy release rates, Int. J. Adhes. Adhes. 32 (2012) 23–38.

[63] F. Sun, R. Zhang, B.R.K. Blackman, Determination of the mode I crack tip opening rate and the rate dependent cohesive properties for structural adhesive joints using digital image correlation, Int. J. Solids Struct. 217-218 (2021) 60–73.